A Wave Model and Diffusion Coefficients for Plasmaspheric Hiss Parameterized by Plasmapause Location

David M. Malaspina [1], Hui Zhu [2], Alexander Drozdov [3]

[1]Laboratory for Atmospheric and Space Physics, University of Colorado, Boulder, Colorado, USA
[2]University of Texas at Dallas, Dallas, Texas, USA
[3]University of California, Los Angeles, Los Angeles, California, USA

Key Points:

- An observation-based wave model for plasmaspheric hiss parameterized by plasmapause location is created
- Corresponding diffusion coefficients are calculated
- Differences between wave models parameterized by plasmapause location and by L-shell are demonstrated via simulations of an idealized storm

Corresponding author: D. M. Malaspina, David.Malaspina@lasp.colorado.edu

Abstract

The scattering of electrons via plasmaspheric hiss whistler-mode plasma waves has profound consequences for the dynamics of electrons in the inner terrestrial magnetosphere, including the radiation belts. Consequently, simulations of inner magnetospheric electron dynamics incorporate hiss wave models, though these models are often parameterized by quantities convenient to describe particle populations (e.g. L-shell). However, recent studies have revealed that the spatial distribution of plasmaspheric hiss wave power is only weakly dependent on L-shell. Instead, it is dictated by the density structure of the plasmasphere (including radial extent and azimuthal structure). In this work, we create a plasmaspheric hiss wave model, and corresponding particle diffusion coefficients, parameterized by plasmapause location instead of L-shell, in order to quantify the importance of including plasmapause-organization of hiss waves for inner magnetosphere models. Significant differences in electron scattering lifetimes are found when comparing L-shell parameterized hiss and plasmapause-parameterized hiss wave models on the timescales of days. This implies that plasmapause-parameterization of hiss waves may be important for modeling specific geomagnetic events.

1 Introduction

Plasmaspheric hiss is a broadband superposition of whistler-mode plasma waves located within and nearby the plasmasphere, a torus of cold plasma surrounding Earth. Hiss scatters electrons in pitch angle, facilitating their loss to the atmosphere and thereby playing a significant role in shaping inner magnetospheric electron populations, including relativistic radiation belt electrons (e.g. see Millan & Thorne, 2007). For this reason, electron loss by hiss wave scattering is a critical component of simulations of the inner magnetosphere (Albert et al., 2009; Fok et al., 2014; Jordanova & Miyoshi, 2005; Miyoshi et al., 2006; Shprits et al., 2008; Subbotin & Shprits, 2009). Simulations often include the physics of hiss-induced particle scattering using statistical maps of hiss wave characteristics (e.g. intensity, spectral shape) parameterized by L-shell, magnetic local time (MLT), and geomagnetic activity level (Glauert et al., 2014; Meredith et al., 2007; Orlova et al., 2014; Tsurutani et al., 2015; Orlova et al., 2016).

Recent studies have demonstrated (Malaspina et al., 2016, 2017) that the plasmasphere plays a larger role in the distribution of plasmaspheric hiss wave power than sim-

ply acting as an outer boundary to wave occurrence (as in Meredith et al. (2007), for example). Instead, it was found that the distribution of hiss wave power dynamically adapts to the shape of the plasmasphere, with the peak hiss intensity consistently located a distance of 1 to 1.5 L-shell Earthward of the plasmapause. Further, Malaspina, Ripoll, Chu, Hospodarsky, and Wygant (2018) demonstrated that the radial variation in hiss wave power is determined by primarily by plasma density and is only weakly related to L-shell.

The finding that hiss waves do not follow the L-shell parameterization that models often assume may be of critical importance for physically accurate modeling of wave-particle interactions by hiss waves in the inner magnetosphere. If the hiss wave power peak is being modeled at an unphysical location and/or with an unphysical amplitude, particle scattering estimates may be significantly affected. Further, the shape of the plasmasphere, and therefore the spatial distribution of hiss wave power, is constantly evolving, dynamically determined by a balance of solar wind-driven convection, co-rotation with Earth's magnetic field, refilling from ionospheric outflow, and the time history of all these processes (Carpenter & Lemaire, 2004).

In this work, we begin quantifying the difference between hiss parameterized by plasmapause location (L_{pp}-sorted) and hiss parameterized by L-shell (L-sorted) for models of hiss wave scattering by: (i) Using Van Allen Probes plasma wave observations to create a database of hiss wave power parameterized by wave frequency, magnetic local time, plasmapause location (using both L_{PP}, the distance of the plasmapause from Earth, and ΔL_{PP}, the distance from the plasmapause), and the Kp geomagnetic index. (ii) Using this observational database to produce a L_{pp}-sorted hiss wave model amenable to calculation of diffusion coefficients. (iii) Producing diffusion coefficients based on the wave model. (iv) Applying the L-sorted and L_{pp}-sorted diffusion coefficients to model an idealized geomagnetic storm using the Versatile Electron Radiation Belt (VERB) code (Subbotin & Shprits, 2009), performing one-dimensional pitch-angle diffusion simulations, and comparing code outputs.

This work focuses on plasmaspheric hiss, defined here as hiss found within the plasmasphere at frequencies between 150 Hz and ∼2 kHz. Other hiss types will be parameterized in future work, including plume hiss (Li et al., 2019), low frequency hiss (Li et al., 2013), lightning hiss (Meredith et al., 2007), and exohiss (Zhu et al., 2015; Zhu et al., 2019). By building a wave model for each hiss type separately, they can be included

or excluded from VERB code runs to quantify their relative importance to inner magnetospheric dynamics.

Section 2 describes the wave data and its processing. Section 3 describes the parameterized wave model built from the observations. Section 4 describes the calculation of diffusion coefficients, and Section 5 treats the VERB modeling. Conclusions are presented in Section 6.

2 Observations

2.1 Data Set Creation

This study uses data from the Van Allen Probes mission (Mauk et al., 2013). These two identical spacecraft have elliptical orbits about the Earth with perigee near 600 km and apogee near 6 Earth radii (R_E). Their orbits are within 20° of the geomagnetic equator and each has an orbital period close to 9 hours. Over ∼2 years, their orbital line of apsides precesses through all MLT. The spacecraft are spin-stabilized with ∼11 s spin period.

Instrument data used in this study are from the Electric Fields and Waves (EFW) instrument (Wygant et al., 2013) and the Electric and Magnetic Field Instrument Suite and Integrated Science (EMFISIS) suite (Kletzing et al., 2013). These instruments record and process measurements made by six electric field probes, a three-axis search coil magnetometer (SCM), and a three-axis fluxgate magnetometer (FGM). The data products used by this study include the spacecraft potential (32 Samples/s), the DC-coupled magnetic field (64 Samples/s), density determined from a combination of the upper hybrid frequency (1 sample / 6.5 s) and spacecraft potential, and on-board calculated wave power spectra of each SCM axis (65 pseudo-logarithmically spaced frequency bins from ∼ 2 Hz to ∼12 kHz, 1 spectra / 6s). Wave planarity and ellipticity data, derived from on-board calculated cross-spectral data (1 spectra / 6s), are also used.

Data from both Van Allen Probes are used. For Van Allen Probe B, data from 01 November, 2012 through 31 January, 2018 are used. For Van Allen Probe A, data from 01 November, 2012 through 31 May, 2016 are used. Data after May 2016 on Van Allen Probe A are not used, as accumulated radiation damage to that spacecraft's electric field sensor preamplifiers compromised their ability to accurately measure spacecraft potential soon after that date.

The Olson-Pfitzer quiet-time magnetic field model (Olson & Pfitzer, 1974) is used to determine L-shell values at any given time and spacecraft location. In general, this model is appropriate at high L-shells ($L > 4.5$) during geomagnetically quiet times and at low L-shells ($L < 4.5$) during both active and quiet times. Plasmaspheric hiss, by definition, remains within the plasmasphere, and so is present at high L-shells during quiet times (extended plasmasphere) and at low L-shells during active times (eroded plasmasphere). Therefore the Olson-Pfitzer quiet-time model is appropriate for plasmaspheric hiss studies. L-shell is used instead of L* because the relevant quantity for plasma waves is their radial distance from Earth (or the plasmapause) at the geomagnetic equator rather than a particle drift invariant (e.g Koller et al., 2009, and references therein).

The plasmapause is identified using the method described in Malaspina et al. (2016). This method uses plasma density derived from spacecraft potential measurements calibrated each orbit against the measured upper hybrid resonance frequency, combined with the Moldwin, Downward, Rassoul, Amin, and Anderson (2002) criteria that density change by 5x or more over 0.5 L-shell. When multiple density gradients satisfying this criteria were found, the one closest to Earth is designated as the plasmapause.

Isolating plasmaspheric hiss wave power from all other phenomenon detected by the Van Allen Probes SCM requires excluding some data from the analysis. Data recorded at $L < 1.6$ were not considered. Data from half-orbits where no plasmapause was detected are excluded because ΔL_{pp} is undefined for those data. Times during spacecraft maneuvers, significant spacecraft surface charging ($|V_{sc}| > 20$V), and times when the spacecraft were in Earth eclipse were removed. Wave power > 2 kHz was excluded, as those higher frequencies contain significant contributions from lightning generated whistler-mode waves (Meredith et al., 2007), which we do not wish to include in the current model. Wave data outside the identified plasmapause L-shell or when the corresponding plasma density measurement was $< 50\text{cm}^{-3}$ were excluded from consideration, to aggressively filter out chorus wave power.

Several filters were applied to the remaining spectral wave data to exclude wave modes not under consideration and to separate signal from noise. Spectral bins dominated by magnetosonic wave power were excluded by removing from consideration spectral data (by time and frequency bin) with high compressability $B_{wave\ ||}\ /\ B_{wave\ total} > 0.6$. Spectral data had to meet the following criteria: planarity > 0.2 and ellipticity $>$

0.7 (Li et al., 2015) and signal to noise ≥ 5 (using the empirical SCM noise function derived in (Malaspina et al., 2017)). The low planarity threshold (0.2) is justified here because planarity is being used only to exclude non-hiss waves (such as magnetosonic waves). A higher planarity threshold (0.5 or greater) would be required if the on-board cross-spectral data were being used to estimate wave vectors. After these exclusions, the remaining database includes 1.9×10^8 spectral data samples.

2.2 Plasmaspheric Hiss Data

The plasmaspheric hiss data examined here are wave power spectral density (units of nT^2/Hz) binned by five quantities: frequency, distance of the plasmapause from Earth (L_{pp}), distance from the plasmapause (ΔL_{pp}), Magnetic Local Time (MLT), and the Kp geomagnetic activity index. The 65 pseudo-logarithmic spaced frequency bins defined by the EMFISIS on-board spectra are used for frequency binning. Four L_{pp} bins are used, covering the range of possible plasmapause locations observable by the Van Allen Probes: $2 \leq L_{pp} < 3$, $3 \leq L_{pp} < 4$, $4 \leq L_{pp} < 5$, and $5 \leq L_{pp}6$. The 25 bins for ΔL_{pp} span a range of -5 to 0, with a bin width of 0.2 L. Six MLT bins with 4 hour width are used: $0 < MLT \leq 4$, $4 < MLT \leq 8$, and so on. Finally, six Kp bins are used, where the first five have a span of 1 Kp (e.g. $0 \leq Kp < 1$, $1 \leq Kp < 2$). The final Kp bin includes Kp ≥ 5. This final bin width was selected to ensure sufficient data for meaningful statistics in this bin. This was necessary because geomagnetic conditions resulting in Kp ≥ 5 are rare during the Van Allen Probes era.

Figure 1 shows mean values of plasmaspheric hiss wave power as a function of frequency and ΔL_{PP} for four different ranges of L_{PP}: Figure 1a $5 < L_{PP} \leq 6$, Figure 1b $4 < L_{PP} \leq 5$, Figure 1c $3 < L_{PP} \leq 4$, Figure 1d $2 < L_{PP} \leq 3$. The data shown are for $8 < MLT \leq 12$ and $1 \leq Kp < 2$, but the data look similar for other MLT and Kp bins. Contours of amplitude are plotted over the amplitude range shown. In each case, the amplitude contours trace an elliptical shape centered at a few hundred Hz in frequency. The data show properties consistent with prior studies (e.g. (Malaspina et al., 2017)): the wave power peaks near 400 Hz, at a radial distance approximately between the Earth and the plasmapause. When the plasmapause is eroded, the wave power is compressed into a smaller radial extent and the amplitude increases.

The thick black horizontal lines indicate 150 Hz. While wave power below 150 Hz is plotted in Figure 1, those data are not used for the plasmaspheric hiss wave model derived in this work. Hiss wave power below 150 Hz is considered low frequency hiss (Li et al., 2013; Ni et al., 2014; Malaspina et al., 2017), and will be considered separately in future work.

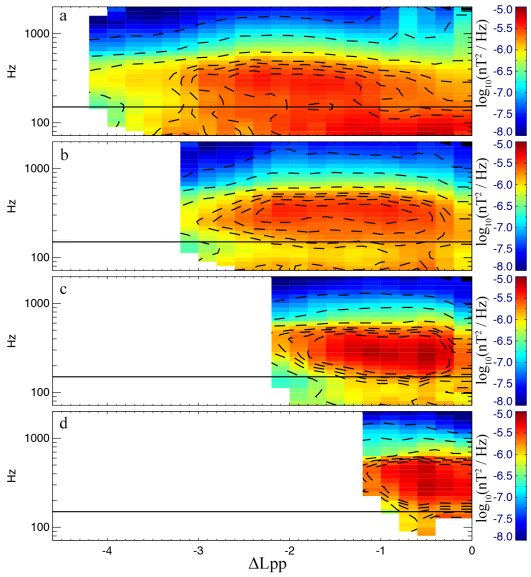

Figure 1. Mean values of observed plasmaspheric hiss wave power as a function of frequency and ΔL_{PP} for four different L_{PP} ranges, $8 < MLT \leq 12$ and $1 \leq Kp < 2$. (a) $5 < L_{PP} \leq 6$. (b) $4 < L_{PP} \leq 5$. (c) $3 < L_{PP} \leq 4$. (d) $2 < L_{PP} \leq 3$. Horizontal black lines indicate 150 Hz. Contour levels are included, indicating levels across the amplitude range shown.

3 Plasmapause-Parameterized Wave Model

Using the plasma wave data collected by the Van Allen Probes as described above, we create a plasmaspheric hiss wave model, parameterized by frequency, L_{pp}, ΔL_{pp}, and Kp.

The shape of hiss wave power spectral density (PSD) profiles with respect to wave frequency are found to depend strongly on L_{pp} and ΔL_{pp}, and weakly on MLT and Kp. PSD profile amplitude is found to vary with L_{pp}, ΔL_{pp}, MLT, and Kp. Therefore, a parameterization is chosen such that the wave model PSD frequency profile shape is determined by L_{pp} and ΔL_{pp}, while the appropriate amplitude scaling for that shape is determined by L_{pp}, ΔL_{pp}, MLT, and Kp.

To create the wave model, PSD data are first averaged over MLT and Kp. Figure 2 shows these averaged PSD vs. frequency profiles (solid lines) as a function of L_{pp} and ΔL_{pp}. When PSD profiles have similar peak frequencies for different ranges of ΔL_{pp} they are combined into a single profile. The resulting PSD frequency-profiles were fit with an analytic function (dotted lines) (a piece-wise 7th order polynomial function) to facilitate diffusion coefficient calculations. Fits are carried out separately for frequency ranges before and after the maxima of the PSD profiles f_{peak} as follows:

$$\text{PSD}(f) = \begin{cases} \sum_{n=0}^{7} a_n f^n & (f < f_{\text{peak}}) \\ \sum_{n=0}^{7} b_n f^n & (f \geq f_{\text{peak}}) \end{cases} \tag{1}$$

We then normalize over the obtained PSD profiles such that the wave amplitude is unity when integrated over the frequency range from 150 Hz to 2000 Hz.

All values of f_{peak} and fitted polynomial coefficients can be found in Table 1. The wave amplitude scaling appropriate to each normalized PSD profiles is obtained by comparison with the observational hiss database. This combination of PSD profile fitting and wave amplitude scaling allows us to fully parameterize the hiss wave distributions.

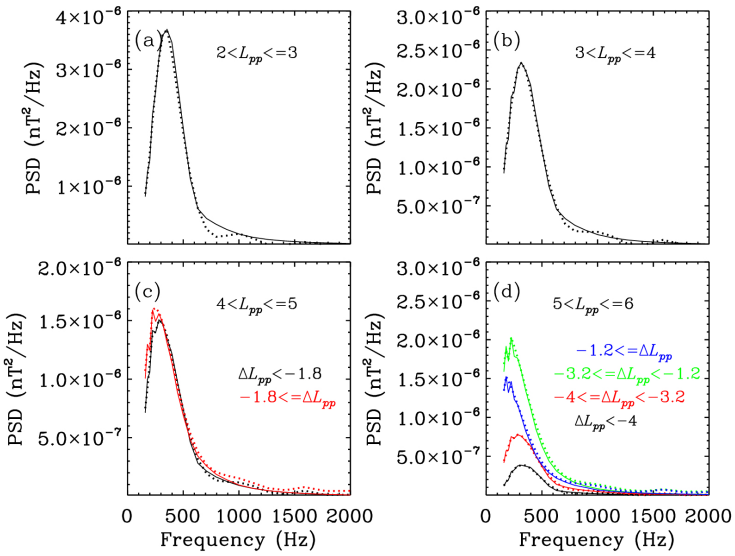

Figure 2. PSD (nT^2/Hz) sorted by L_{pp} and ΔL_{pp} (solid lines) and 7th order polynomial piece-wise fitting (dotted lines), for four ranges of L_{pp} (a-d) and ΔL_{pp}

.

Figure 3 shows the comparison between the observed and parameterized hiss wave power distributions and their normalized difference as functions of ΔL_{pp} and L_{pp}. The normalized difference is defined as

$$\mathrm{ND}(f, dL_{pp}) = \frac{2\left(PSD_{fitted}(f, \Delta L_{pp}) - PSD_{observed}(f, \Delta L_{pp})\right)}{max\left(PSD_{fitted}(f, \Delta L_{pp}) + PSD_{observed}(f, \Delta L_{pp})\right)|_f} \tag{2}$$

It is shown that the observed PSD distributions of hiss wave power are well-modeled by the fitting results and the normalized differences between the fits and observations are close to zero.

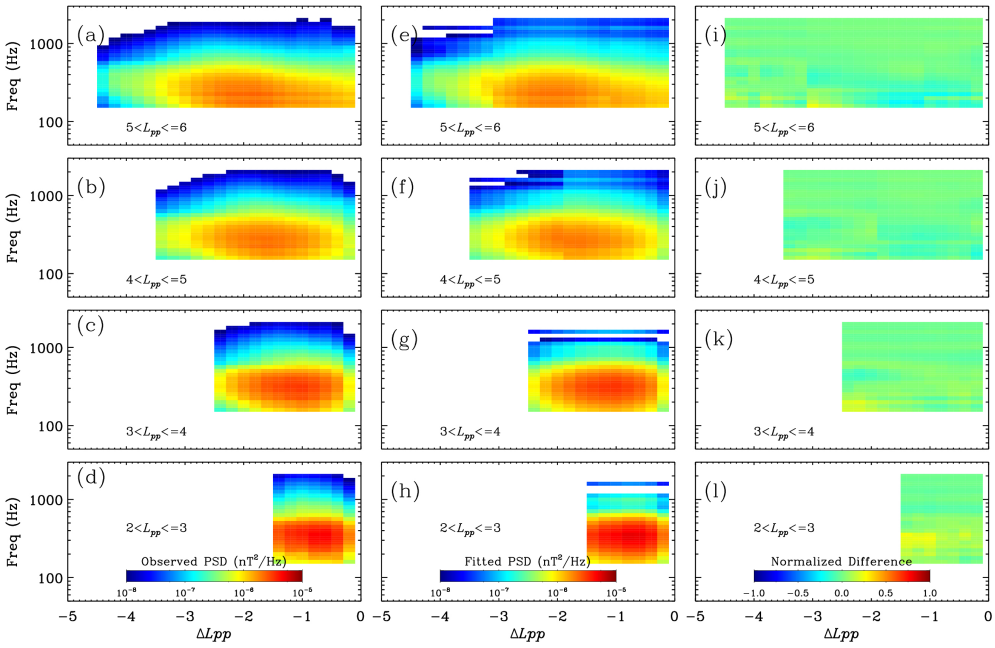

Figure 3. Observed (a-d) and fitted (e-h) power spectral density distributions of plasmaspheric hiss waves and their normalized difference (i-l) as function of ΔL_{pp} and L_{pp} averaged over MLT and Kp

In addition to the L_{pp}-sorted wave model, a traditional hiss wave model was constructed based on the same wave data (parameterized by L-shell, instead of ΔL_{pp} and L_{pp}). PSD frequency profiles and amplitude scalings were obtained using methodology analogous to that described for the L_{pp}-sorted model.

4 Diffusion Coefficient Calculations

The Full Diffusion Code (FDC) (Ni et al., 2008; Shprits & Ni, 2009) is used to calculate plasmaspheric hiss diffusion coefficients. The polynomial fits of the observed L_{pp}-sorted hiss PSD profiles described in Section 3 are used as frequency inputs into the code. The Denton et al. (2006) model is used to define plasma number density. The wave normal distribution is assumed to be a Gaussian distribution (Glauert & Horne, 2005) with a peak at tan(0°), a width tan(30°), a lower cutoff tan(0°) and an upper cutoff tan(45°). The resonance orders from -5 to 5, including 0 order, are considered.

Diffusion matrices at specific values of L-shell and Kp-index are multiplied by the hiss wave amplitude scaling factors determined for the corresponding L_{pp}, ΔL_{pp}, and Kp. Diffusion matrices are averaged over MLT. Using analogous methodology, diffusion coefficients are also calculated for the L-sorted hiss wave model PSD profiles.

Figures 4a, b, e, f show an example of calculated pitch-angle ($D_{\alpha\alpha}$), energy (D_{pp}), mixed ($D_{\alpha p}$) diffusion coefficients, as well as the the sign of the mixed term, for the L_{pp}-sorted hiss model at fixed $L = 3.5$, $Kp = 2$ and $3 < L_{pp} \leq 4$. As expected, the energy diffusion coefficient of the hiss waves is relatively small in comparison to the pitch angle diffusion coefficient. Figure 4c shows the pitch angle diffusion coefficient at the same L-shell and Kp-index but for a different plasmapause location $4 < L_{pp} \leq 5$. The difference between pitch angle diffusion coefficients (Figure 4g, difference between Figure 4a and Figure 4c) indicates that stronger scattering by hiss waves when the plasmapause is closer Earth primarily affects electrons with energies from 100 keV to 1 MeV.

Figure 4d shows pitch angle diffusion coefficients for the hiss model constructed using traditional L-sorted methodology. The difference between pitch angle diffusion coefficients from L_{pp}-sorted and L-sorted models (Figure 4h, difference between 4a and 4d) is clear, for the same range of electron energies. The differences reach $\sim 2\ days^{-1}$. Thus, the one can expect that electron distribution dynamics in diffusion simulations will depend on the wave data parameterization (sorting) approach of the hiss model (L-sorted vs L_{pp}-sorted). In addition, the variation can be significant on the timescales of geomagnetic storms (a few days).

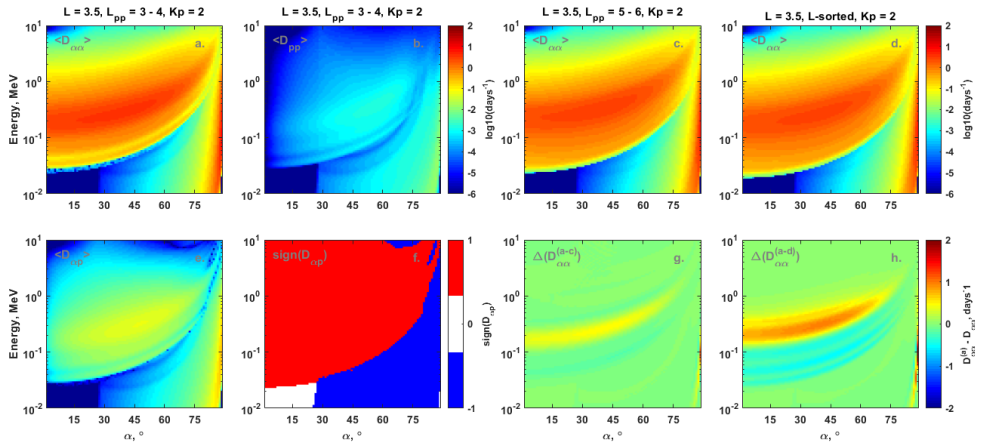

Figure 4. (a,b,e) Calculated diffusion coefficients for L_{pp}-sorted plasmaspheric hiss waves model $3 < L_{pp} \leq 4$, (f) Sign of $D_{\alpha p}$, (c) $D_{\alpha\alpha}$, $5 < L_{pp} \leq 6$, (d) $D_{\alpha\alpha}$, L-sorted hiss model. (g, h) Difference of panels c and d with panel a.

5 Pitch angle diffusion simulations

To quantify the impact of the wave data sorting approach on modeling results, we perform VERB code simulations in 1D mode using pitch-angle diffusion only. This approach allows us to focus on the impact that different hiss wave models may have on the simulation as we ignore other processes such as radial diffusion. Since the electron acceleration by hiss waves is ineffective, we ignore energy diffusion. Neglecting radial and energy diffusion, the Fokker-Planck equation (Schulz & Lanzerotti, 1974) that describes the evolution phase space density (f) can be written as:

$$\frac{\partial f}{\partial t} = \frac{1}{T(\sin(\alpha))sin(2\alpha)} \frac{\partial}{\partial \alpha} T(\sin(\alpha))sin(2\alpha) D_{\alpha\alpha} \frac{\partial f}{\partial \alpha} - \frac{f}{\tau}$$

where $T(\sin(\alpha)) \approx 1.38 - 0.32(\sin(\alpha) + \sqrt{\sin(\alpha)})$ is a function that corresponds to the bounce frequency, approximated following Lenchek, Singer, and Wentworth (1961), α is the equatorial pitch angle, $D_{\alpha\alpha}$ is the pitch angle diffusion coefficient, τ defines the lifetime of the particle inside the loss cone where it is equal to quarter of the bounce period.

We perform simulations on a grid of $\alpha \in [0.1°, 89.5°]$ linearly distributed among 101 points. The Dirichlet boundary condition is equal to zero at $\alpha = 0.1°$ and the Neumann boundary condition is the derivative equal to zero at $\alpha = 89.5°$. The initial condition is an isotropic phase space density distribution ($f(\alpha) = 1$). The energy of the

electrons is 1 MeV. A similar simulation setup was used in previous studies (e.g. Shprits et al., 2009).

Figure 5 shows the results of two simulations at fixed L-shell equal to 3.5. These simulations are distinguished by the use of two models for hiss waves described above (L-sorted and L_{pp}-sorted). Different diffusion coefficients are applied for each wave model. Both simulations were performed for 7 days, using a prescribed variation of the Kp-index during an idealized geomagnetic storm (Figure 5a). The plasmapause location is determined based on Kp following Carpenter and Anderson (1992) (Figure 5b).

To compare the results of the simulations, decay rates are calculated at different pitch angles ($20°, 60°, 89°$ in Figures 5c, f) and overall decay times are calculated following the technique described in Shprits, Li, and Thorne (2006) (Figures 5e, h). The decay rates are controlled by the electron phase space density gradient and the diffusion rate at the edge of the loss cone (see Shprits et al., 2006).

Both simulations are given an initial 4 day period of constant $Kp = 2$, which corresponds to a constant location of the plasmapause at $L_{pp} = 4.68$. During this period, the diffusion coefficients are held constant in both simulations as the simulations reach steady state conditions (no change in phase space density gradient, see Figure 5c, d). Hence, the electron dynamics of the remainder of the modeled time period are defined by variation of the diffusion coefficients, which are determined by the wave data sorting approach, L_{pp}- vs L-sorted). The idealized geomagnetic storm starts on day 4 with increasing Kp-index and corresponding compression of the plasmapause spanning one day. On day 5, the Kp-index is allowed to decrease, followed by an expansion of the plasmapause on day 6. Such conditions are typical for geomagnetic storms.

Comparison of the simulation results shows that the electron decay rate evolution during the storm time is noticeably different (see Figure 5c, f). The difference is also visible in evolution of the phase space density profiles for 1 MeV electrons (see Figure 5d, g). The step-like increases of decay rate in Figure 5f are the consequence of the small number (4) of discrete L_{pp} bins that are used to calculate the diffusion coefficients. The small number of bins is due to statistical limitations of the wave data. The presence of these steps does not alter the clear difference in the simulated electron dynamics found by using different hiss models.

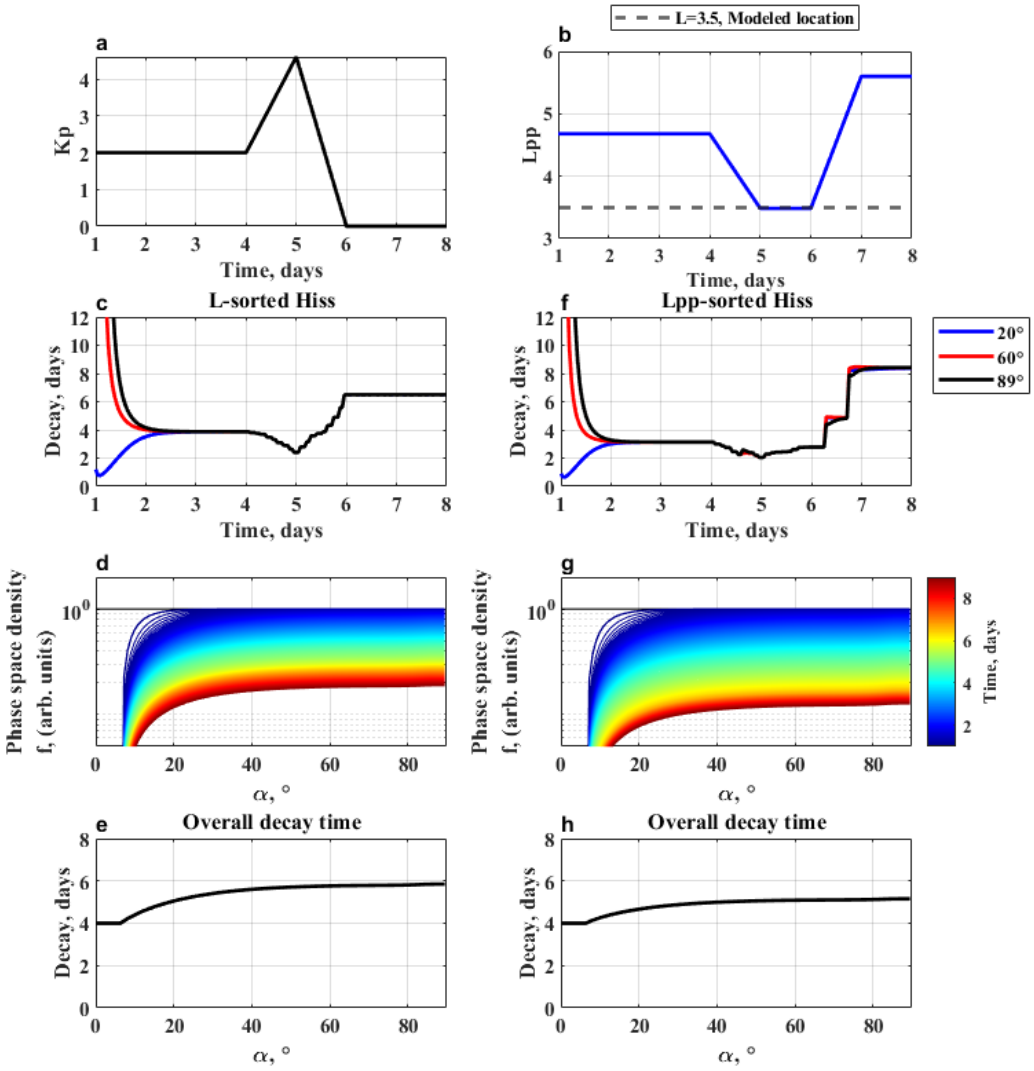

Figure 5. One-dimensional modeling of idealized geomagnetic storm at L=3.5. (a) Kp-index. (b) Location of the plasmapause. (c, d, e) Results of the simulation with the L-sorted hiss model. (f, g, h) Results of the simulation with the L_{pp}-sorted hiss model. (c, f) Evolution of decay time during the storm. (d, g) Evolution of the pitch angle distribution for 1 MeV electrons (phase space density). (e, h) Overall decay time as a function of the equatorial pitch angle, calculated using initial and final phase space density profiles.

Based on these results, it is expected that a simulation of a realistic storm using the L_{pp}-sorted hiss model will result in different electron dynamics on the time scale of the duration of the storm (days) compared to simulations using traditional L-sorted hiss

wave models. Simulations using the L_{pp}-sorted hiss model may reveal otherwise-hidden variation of the electron distribution during storms and may also lead to a different simulated balance between acceleration and loss processes due to changes in the phase space density gradient. However, pitch angle scattering by hiss waves is only one of many processes that define the dynamics of the electrons. Future simulations will include contributions from other very low frequency (VLF) waves via pitch-angle, energy, mixed diffusion, and radial diffusion driven by ultra-low frequency (ULF) waves.

6 Conclusion

In this study, Van Allen Probes observations of plasmaspheric hiss (organized by frequency, ΔL_{pp}, L_{pp}, MLT, and K_p) were compiled for the time period 2012 - 2018. From these data, an empirical hiss wave model was constructed for hiss parameterized by ΔL_{pp}, L_{PP}, and K_p. Corresponding pitch-angle and energy diffusion coefficients (including mixed-terms) were calculated.

The pitch angle diffusion coefficients for the L_{pp}-sorted empirical hiss model showed significant differences when compared with diffusion coefficients calculated for the same L-shell but using traditional L-sorted hiss parameterization.

A 1D mode of the VERB code with idealized geomagnetic storm conditions was used to quantify differences in electron lifetimes as determined using diffusion coefficients calculated using the L_{pp}-sorted hiss wave model and the L-sorted hiss wave model. Clear differences were found over time timescales of the geomagnetic storm (few days).

Future studies will expand upon the current model by (i) simulating more realistic geomagnetic variation time-histories, (ii) utilizing the 3D mode of the VERB code, and (iii) developing L_{pp}-sorted parameterizations for other hiss types such as exohiss and low frequency hiss.

Acknowledgments

The authors thank the Van Allen Probes team, especially the EFW and EMFISIS teams for their support. This work was funded by NASA grant 80NSSC18K1034. All Van Allen Probes data used in this work are available from the EFW and EMFISIS team websites, which one can link to here: http://rbspgway.jhuapl.edu. The diffusion coefficients, wave amplitude scaling, and the VERB code are available on ftp://rbm.epss.ucla.edu/.

Table 1. The values of $f_{\rm peak}$ and the fitted polynomial coefficients of plasmaspheric hiss waves as functions of L_{pp} and ΔL_{pp}.

L_{pp} ranges	ΔL_{pp} ranges	$f_{\rm peak}$ (Hz)	a_0	a_1	a_2	a_3	a_4	a_5	a_6	a_7
			b_0	b_1	b_2	b_3	b_4	b_5	b_6	b_7
$2 < L_{pp} \leq 3$	$\Delta L_{pp} < 0$	355	6.59e-3	-3.41e-4	6.98e-6	-7.24e-8	4.19e-10	-1.35e-12	2.29e-15	-1.58e-18
			-2.99e-2	3.17e-4	-1.15e-6	2.05e-9	-2.02e-12	1.13e-15	-3.33e-19	4.04e-23
$3 < L_{pp} \leq 4$	$\Delta L_{pp} < 0$	316	9.29e-3	-4.81e-4	1.01e-5	-1.08e-7	6.64e-10	-2.31e-12	4.25e-15	-3.22e-18
			-1.97e-2	2.16e-4	-7.88e-7	1.41e-9	-1.39e-12	7.79e-16	-2.30e-19	2.78e-23
$4 < L_{pp} \leq 5$	$\Delta L_{pp} < -1.8$	282	-2.23e-2	1.29e-3	-2.93e-5	3.54e-7	-2.45e-9	9.76e-12	-2.08e-14	1.83e-17
			-1.18e-2	1.46e-4	-5.50e-7	9.97e-10	-9.92e-13	5.55e-16	-1.64e-19	1.99e-23
$4 < L_{pp} \leq 5$	$-1.8 \leq \Delta L_{pp} < 0$	224	-8.68e-2	5.41e-3	-1.39e-4	1.94e-6	-1.56e-8	7.31e-11	-1.85e-13	1.95e-16
			-4.46e-3	7.73e-5	-3.13e-7	5.86e-10	-5.96e-13	3.39e-16	-1.01e-19	1.24e-23
$5 < L_{pp} \leq 6$	$\Delta L_{pp} < -4$	316	8.31e-3	-4.30e-4	8.76e-6	-9.13e-8	5.35e-10	-1.77e-12	3.07e-15	-2.19e-18
			-2.96e-2	3.00e-4	-1.07e-6	1.88e-9	-1.85e-12	1.03e-15	-3.02e-19	3.65e-23
$5 < L_{pp} \leq 6$	$-4 \leq \Delta L_{pp} < -3.2$	282	-2.00e-2	1.11e-3	-2.53e-5	3.07e-7	-2.14e-9	8.55e-12	-1.83e-14	1.61e-17
			-1.28e-2	1.56e-4	-5.87e-7	1.07e-9	-1.07e-12	5.98e-16	-1.77e-19	2.15e-23
$5 < L_{pp} \leq 6$	$-3.2 \leq \Delta L_{pp} < -1.2$	224	-1.09e-1	6.90e-3	-1.80e-4	2.51e-6	-2.04e-8	9.60e-11	-2.43e-13	2.57e-16
			7.76e-4	3.57e-5	-1.84e-7	3.78e-10	-4.03e-13	2.37e-16	-7.23e-20	8.99e-24
$5 < L_{pp} \leq 6$	$-1.2 \leq \Delta L_{pp} < 0$	178	8.33e-2	-4.39e-3	8.88e-5	-7.95e-7	1.95e-9	1.74e-11	-1.29e-13	2.52e-16
			1.80e-3	2.68e-5	-1.62e-7	3.61e-10	-4.08e-13	2.50e-16	-7.92e-20	1.02e-23

manuscript submitted to *JGR-Space Physics*

References

Albert, J. M., Meredith, N. P., & Horne, R. B. (2009). Three-dimensional diffusion simulation of outer radiation belt electrons during the 9 october 1990 magnetic storm. *J. Geophys. Res. [Space Phys]*, *114*(A9). doi: 10.1029/2009JA014336

Carpenter, D. L., & Anderson, R. R. (1992, February). An ISEE/Whistler model of equatorial electron density in the magnetosphere. *Journal of Geophysical Research (Space Physics)*, *97*, 1097-1108. doi: 10.1029/91JA01548

Carpenter, D. L., & Lemaire, J. (2004, December). The Plasmasphere Boundary Layer. *Annales Geophysicae*, *22*, 4291-4298. doi: 10.5194/angeo-22-4291-2004

Denton, R. E., Takahashi, K., Galkin, I. A., Nsumei, P. A., Huang, X., Reinisch, B. W., ... Hughes, W. J. (2006). Distribution of density along magnetospheric field lines. *J. Geophys. Res.*, *111*, A04213. doi: 10.1029/2005JA011414

Fok, M.-C., Buzulukova, N. Y., Chen, S.-H., Glocer, A., Nagai, T., Valek, P., & Perez, J. D. (2014, September). The Comprehensive Inner Magnetosphere-Ionosphere Model. *Journal of Geophysical Research (Space Physics)*, *119*, 7522-7540. doi: 10.1002/2014JA020239

Glauert, S. A., & Horne, R. B. (2005). Calculation of pitch angle and energy diffusion coefficients with the padie code. *Journal of Geophysical Research: Space Physics*, *110*(A4).

Glauert, S. A., Horne, R. B., & Meredith, N. P. (2014, January). Three-dimensional electron radiation belt simulations using the BAS Radiation Belt Model with new diffusion models for chorus, plasmaspheric hiss, and lightning-generated whistlers. *Journal of Geophysical Research (Space Physics)*, *119*, 268-289. doi: 10.1002/2013JA019281

Jordanova, V. K., & Miyoshi, Y. (2005, 28 July). Relativistic model of ring current and radiation belt ions and electrons: Initial results: RADIATION BELT IONS AND ELECTRONS. *Geophys. Res. Lett.*, *32*(14). doi: 10.1029/2005GL023020

Kletzing, C. A., Kurth, W. S., Acuna, M., MacDowall, R. J., Torbert, R. B., Averkamp, T., ... Tyler, J. (2013, November). The Electric and Magnetic Field Instrument Suite and Integrated Science (EMFISIS) on RBSP. *Space Science Reviews*, *179*, 127-181. doi: 10.1007/s11214-013-9993-6

Koller, J., Reeves, G. D., & Friedel, R. H. W. (2009, Feb). LANL* V1.0: a radiation

belt drift shell model suitable for real-time and reanalysis applications. *Geoscientific Model Development Discussions*, *2*(1), 159-184.

Lenchek, A. M., Singer, S. F., & Wentworth, R. C. (1961, Dec). Geomagnetically Trapped Electrons from Cosmic-Ray Albedo Neutrons. *Journal of Geophysical Research*, *66*(12), 4027-4046. doi: 10.1029/JZ066i012p04027

Li, W., Ma, Q., Thorne, R. M., Bortnik, J., Kletzing, C. A., Kurth, W. S., ... Nishimura, Y. (2015, May). Statistical properties of plasmaspheric hiss derived from Van Allen Probes data and their effects on radiation belt electron dynamics. *Journal of Geophysical Research (Space Physics)*, *120*, 3393-3405. doi: 10.1002/2015JA021048

Li, W., Shen, X. C., Ma, Q., Capannolo, L., Shi, R., Redmon, R. J., ... Hospodarsky, G. B. (2019, Apr). Quantification of Energetic Electron Precipitation Driven by Plume Whistler Mode Waves, Plasmaspheric Hiss, and Exohiss. *Geophysical Research Letters*, *46*(7), 3615-3624. doi: 10.1029/2019GL082095

Li, W., Thorne, R. M., Bortnik, J., Reeves, G. D., Kletzing, C. A., Kurth, W. S., ... Thaller, S. A. (2013, August). An unusual enhancement of low-frequency plasmaspheric hiss in the outer plasmasphere associated with substorm-injected electrons. *Geophysical Review Letters*, *40*, 3798-3803. doi: 10.1002/grl.50787

Malaspina, D. M., Jaynes, A. N., Boulé, C., Bortnik, J., Thaller, S. A., Ergun, R. E., ... Wygant, J. R. (2016, August). The distribution of plasmaspheric hiss wave power with respect to plasmapause location. *Geophysical Review Letters*, *43*, 7878-7886. doi: 10.1002/2016GL069982

Malaspina, D. M., Jaynes, A. N., Hospodarsky, G., Bortnik, J., Ergun, R. E., & Wygant, J. (2017, August). Statistical properties of low-frequency plasmaspheric hiss. *Journal of Geophysical Research (Space Physics)*, *122*, 8340-8352. doi: 10.1002/2017JA024328

Malaspina, D. M., Ripoll, J.-F., Chu, X., Hospodarsky, G., & Wygant, J. (2018, September). Variation in Plasmaspheric Hiss Wave Power With Plasma Density. *Geophysical Research Letters*, *45*, 9417-9426. doi: 10.1029/2018GL078564

Mauk, B. H., Fox, N. J., Kanekal, S. G., Kessel, R. L., Sibeck, D. G., & Ukhorskiy, A. (2013, November). Science Objectives and Rationale for the Radiation Belt Storm Probes Mission. *Space Science Reviews*, *179*, 3-27. doi:

10.1007/s11214-012-9908-y

Meredith, N. P., Horne, R. B., Glauert, S. A., & Anderson, R. R. (2007, August). Slot region electron loss timescales due to plasmaspheric hiss and lightning-generated whistlers. *Journal of Geophysical Research (Space Physics)*, *112*, 8214. doi: 10.1029/2007JA012413

Millan, R. M., & Thorne, R. M. (2007, March). Review of radiation belt relativistic electron losses. *Journal of Atmospheric and Solar-Terrestrial Physics*, *69*, 362-377. doi: 10.1016/j.jastp.2006.06.019

Miyoshi, Y. S., Jordanova, V. K., Morioka, A., Thomsen, M. F., Reeves, G. D., Evans, D. S., & Green, J. C. (2006, 1 November). Observations and modeling of energetic electron dynamics during the october 2001 storm. *J. Geophys. Res.*, *111*(A11), A11S02. doi: 10.1029/2005JA011351

Moldwin, M. B., Downward, L., Rassoul, H. K., Amin, R., & Anderson, R. R. (2002, November). A new model of the location of the plasmapause: CRRES results. *Journal of Geophysical Research (Space Physics)*, *107*, 1339. doi: 10.1029/2001JA009211

Ni, B., Li, W., Thorne, R. M., Bortnik, J., Ma, Q., Chen, L., ... Claudepierre, S. G. (2014, March). Resonant scattering of energetic electrons by unusual low-frequency hiss. *Geophysical Review Letters*, *41*, 1854-1861. doi: 10.1002/2014GL059389

Ni, B., Thorne, R. M., Shprits, Y. Y., & Bortnik, J. (2008). Resonant scattering of plasma sheet electrons by whistler-mode chorus: Contribution to diffuse auroral precipitation. *Geophysical Research Letters*, *35*(11). Retrieved from `https://agupubs.onlinelibrary.wiley.com/doi/abs/10.1029/2008GL034032` doi: 10.1029/2008GL034032

Olson, W. P., & Pfitzer, K. A. (1974). A quantitative model of the magnetospheric magnetic field. *Journal of Geophysical Research (Space Physics)*, *79*, 3739. doi: 10.1029/JA079i025p03739

Orlova, K., Shprits, Y., & Spasojevic, M. (2016, February). New global loss model of energetic and relativistic electrons based on Van Allen Probes measurements. *Journal of Geophysical Research (Space Physics)*, *121*, 1308-1314. doi: 10.1002/2015JA021878

Orlova, K., Spasojevic, M., & Shprits, Y. (2014, June). Activity-dependent global

435 model of electron loss inside the plasmasphere. *Geophysical Review Letters*, *41*,
436 3744-3751. doi: 10.1002/2014GL060100

437 Schulz, M., & Lanzerotti, L. J. (1974). *Particle diffusion in the radiation belts.*

438 Shprits, Y. Y., Chen, L., & Thorne, R. M. (2009). Simulations of pitch angle scat-
439 tering of relativistic electrons with mlt-dependent diffusion coefficients. *Journal*
440 *of Geophysical Research: Space Physics*, *114*(A3). Retrieved from `https://`
441 `agupubs.onlinelibrary.wiley.com/doi/abs/10.1029/2008JA013695` doi:
442 10.1029/2008JA013695

443 Shprits, Y. Y., Li, W., & Thorne, R. M. (2006). Controlling effect of the pitch an-
444 gle scattering rates near the edge of the loss cone on electron lifetimes. *Journal*
445 *of Geophysical Research: Space Physics*, *111*(A12). Retrieved from `https://`
446 `agupubs.onlinelibrary.wiley.com/doi/abs/10.1029/2006JA011758` doi:
447 10.1029/2006JA011758

448 Shprits, Y. Y., & Ni, B. (2009). Dependence of the quasi-linear scattering
449 rates on the wave normal distribution of chorus waves. *Journal of Geo-*
450 *physical Research: Space Physics*, *114*(A11). Retrieved from `https://`
451 `agupubs.onlinelibrary.wiley.com/doi/abs/10.1029/2009JA014223` doi:
452 10.1029/2009JA014223

453 Shprits, Y. Y., Subbotin, D. A., Meredith, N. P., & Elkington, S. R. (2008, Novem-
454 ber). Review of modeling of losses and sources of relativistic electrons in the
455 outer radiation belt II: Local acceleration and loss. *Journal of Atmospheric*
456 *and Solar-Terrestrial Physics*, *70*, 1694-1713. doi: 10.1016/j.jastp.2008.06.014

457 Subbotin, D. A., & Shprits, Y. Y. (2009, October). Three-dimensional modeling of
458 the radiation belts using the Versatile Electron Radiation Belt (VERB) code.
459 *Space Weather*, *7*, S10001. doi: 10.1029/2008SW000452

460 Tsurutani, B. T., Falkowski, B. J., Pickett, J. S., Santolik, O., & Lakhina, G. S.
461 (2015, January). Plasmaspheric hiss properties: Observations from Po-
462 lar. *Journal of Geophysical Research (Space Physics)*, *120*, 414-431. doi:
463 10.1002/2014JA020518

464 Wygant, J. R., Bonnell, J. W., Goetz, K., Ergun, R. E., Mozer, F. S., Bale, S. D.,
465 ... Tao, J. B. (2013, November). The Electric Field and Waves Instruments
466 on the Radiation Belt Storm Probes Mission. *Space Science Reviews*, *179*,
467 183-220. doi: 10.1007/s11214-013-0013-7

Zhu, H., Gu, W., & Chen, L. (2019). Statistical analysis on plasmatrough exohiss waves from the van allen probes. *Journal of Geophysical Research: Space Physics*, *124*(6), 4356–4364.

Zhu, H., Su, Z., Xiao, F., Zheng, H., Wang, Y., Shen, C., ... Baker, D. N. (2015, February). Plasmatrough exohiss waves observed by Van Allen Probes: Evidence for leakage from plasmasphere and resonant scattering of radiation belt electrons. *Geophysical Review Letters*, *42*, 1012-1019. doi: 10.1002/2014GL062964